ARTICLE   OPEN

Check for updates

Observed decreasing trend in the upper-tropospheric cloud top temperature

Huan Liu [ID][1], Ilan Koren [ID][1 ✉] and Orit Altaratz [ID][1]

Obtaining the response of cloud top temperature (CTT) to global warming correctly is crucial for understanding the current and future energy budget of the climate system. For a given cloud fraction, colder CTT implies more longwave radiation being capped within the Earth-atmosphere system, consequently heating it. Current climate models predict an almost fixed CTT for upper-tropospheric clouds as the climate is expected to warm up during the 21st century, as explained by the fixed anvil temperature hypothesis. However, our analysis, based on the last 19 years of satellite observations (12.2002–11.2021), reveals a significant decreasing trend in upper-tropospheric CTT with almost no change in the corresponding cloud fraction. This cooling rate is several times larger than the observed surface warming rate. This finding suggests a missing heating component by upper-tropospheric clouds in current climate predictions.

INTRODUCTION

Cloud top temperature (CTT) is a major climatic factor that, together with the cloud fraction (CF), determines, to a large extent, the thermal emission of the Earth-atmosphere system[1]. Less longwave radiation escapes into space with colder CTT, leading to more energy being trapped within the atmosphere, hence heating it. A decreasing trend in CTT following global warming indicates additional heating of the climate system, i.e., positive feedback[2]. Therefore, information about changes in CTT is crucial for climate prediction. Numerous studies were dedicated to exploring clouds' response to a warmer climate. Among them, current climate models suggest an almost fixed or slightly increased top temperature of upper-tropospheric clouds[2–4], as explained by the fixed anvil temperature (FAT) hypothesis[5] and the proportionally higher anvil temperature (PHAT) hypothesis[6]. This prediction has been identified as highly confident in the latest Intergovernmental Panel on Climate Change Assessment Report (AR6) and has become well-accepted[2].

The FAT hypothesis suggests that the temperature of tropical anvils will not change under climate warming[5]. The physics behind this hypothesis is based on the principles of the tropospheric energy balance, the Clausius-Clapeyron relation, and mass continuity[7]. To elaborate, clear-sky radiative cooling, attributed mainly to longwave emission by water vapor, is balanced by adiabatic heating through subsidence[5,7]. The Clausius-Clapeyron equation relates the amount of water vapor, and hence the tropospheric cooling with height, to the temperature[7,8]. Above a certain level in the troposphere, where the temperature is too cold to contain optically thick amounts of water vapor, the cooling, and accompanying subsidence become inefficient sharply (and hence weaker), leading to a strong clear-sky convergence at this level[5,7]. Due to mass continuity, the strong convergence is balanced by a strong cloudy-sky divergence. Therefore, the anvils and cirrus clouds associated with it are expected to form primarily at this isotherm level, independent of surface warming[5]. The FAT hypothesis was later expanded to the whole globe by demonstrating that the extratropical atmosphere is controlled by similar fundamental physics[9].

Although the FAT hypothesis includes a long chain of assumptions, its general idea is supported by simulations of cloud-resolving models, e.g., ref. [10], and observations focusing on inter-annual variations (e.g., the El Niño–Southern Oscillation, ENSO)[11,12]. These studies agree with the constraint of radiative cooling on anvils' temperature and show its negligible response to surface warming[9–14]. Following this understanding, the FAT hypothesis was refined to the PHAT hypothesis to explain the positive longwave cloud feedback predicted by most of the global climate models (GCMs)[6]. The PHAT hypothesis suggests a slightly increased upper-tropospheric CTT in a warmer climate by taking into account the stronger static stability at higher levels of the upper troposphere (i.e., the stronger the static stability, the weaker the subsidence required to maintain energy balance)[6]. However, there are also simulations[7] and short-term observations (months to years)[15–18] indicating non-negligible changes in anvil temperature with respect to the changes in surface temperature. Additionally, global warming has led to other substantial global changes besides the surface temperature, such as humidity[19]. Direct, long-term observational evidence supporting the FAT or PHAT hypotheses, or disproving them, is still missing[20,21].

Here, to explore the trend in upper-tropospheric CTT, we performed a detailed, almost global (60° S–60° N) analysis on 19 years of daily measurements (12.2002–11.2021) by the MODerate Resolution Imaging Spectroradiometer (MODIS)[22,23] aboard Aqua satellite[24]; MYD08-D3 (Collection 6.1), hereafter MYD08-D3-C6.1[25] (see Data in the Methods section for details). We used this product since it is well-calibrated, and the satellite did not drift during the analysis period[26]. Additionally, single-sensor data avoids discontinuities that may arise when combining datasets from different sources and time periods[27].

RESULTS

Climatology of upper-tropospheric clouds

We start by examining the favorable locations of upper-tropospheric clouds around the globe and their mean CTT. Their mean CF is presented on a global map in Fig. 1a. This subset of

[1]Department of Earth and Planetary Sciences, Weizmann Institute of Science, 76100 Rehovot, Israel. ✉email: ilan.koren@weizmann.ac.il

(a) Upper-tropospheric CF climatology (%)

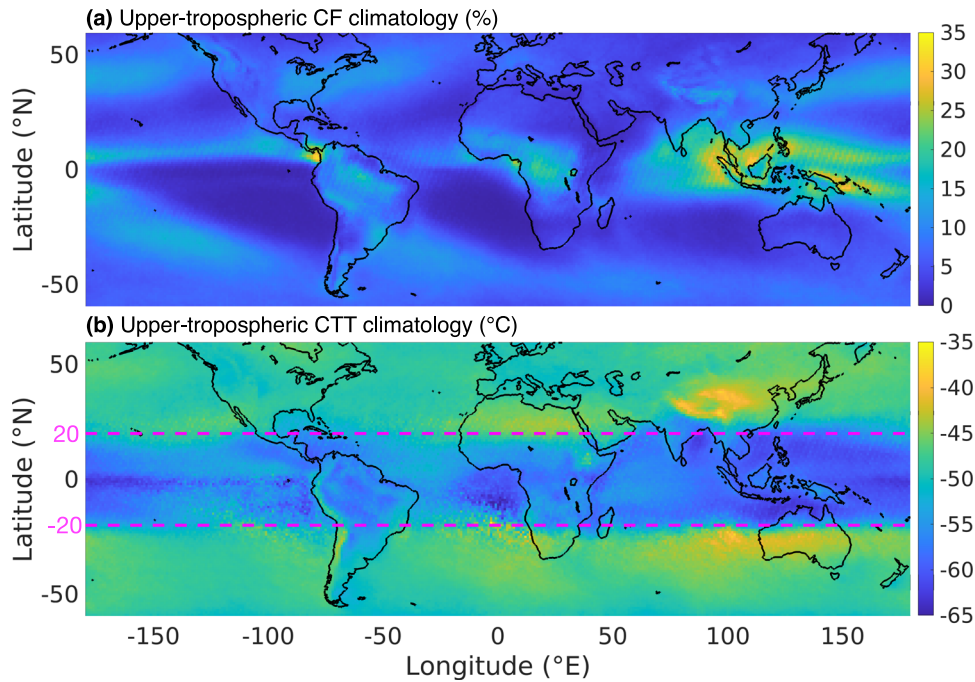**(b) Upper-tropospheric CTT climatology (°C)**

Fig. 1   Maps of CF and CTT mean values for upper-tropospheric clouds, calculated using daily measurements during 12.2002–11.2021. **a** CF mean values, and **b** CTT mean values (CF-weighted). The magenta dashed lines in panel **b** highlight the boundaries of tropical latitudes used in Fig. 3g–i (20° S–20° N, estimated as the boundaries of the very low upper-tropospheric CTT band).

clouds is determined using daily measurements of maximal cloud top pressure (CTP-Max ≤ 450 hPa, see Cloud and Domain Classification in the Methods section for details). Greenish to yellowish colors mark areas with a relatively large CF of upper-tropospheric clouds (>20%), indicating regions with favorable conditions for deep or high cloud formation. Figure 1b presents a global map of the mean upper-tropospheric CTT, exhibiting clear zonal patterns that are consistent with the known areas of deep convection[28] and extratropical cyclones[29].

Previous studies suggested clear land-ocean contrast in atmospheric warming rate and in changes in low-level humidity and CF during recent decades[19,30]. Consequently, we separated the analysis into three domains; D_{global} (60° S–60° N), D_{ocean} (oceans over 60° S–60° N), and D_{land} (continents over 60° S–60° N); see Cloud and Domain Classification in the Methods section. The area covered by upper-tropospheric clouds as a function of their CTT over the whole study period is presented in Fig. 2a–c by gray bars (right y-axis). The corresponding distribution points to a maximal CTT of approximately −20 °C and a mode at approximately –50 °C (marked by magenta lines). It indicates that the subset of analyzed clouds is composed of ice-top clouds reaching the upper part of the troposphere.

Decreasing trend in upper-tropospheric CTT

To demonstrate how the upper-tropospheric CTT changes with time, the normalized distributions representing the first and last 6 years of data are displayed on top of the overall ones (blue and red lines in Fig. 2a–c, left y-axis). In addition, we present the differences in these normalized distributions (last-6 years minus first-6 years, Fig. 2d–f) to highlight the change in upper-tropospheric CTT and avoid potential biases from changing CF and the observing system's performance. The increased normalized frequencies of CTT colder than approximately –65 °C and the decreased normalized frequency of CTT warmer than about –50 °C are consistent over all domains, indicating a shift of the overall upper-tropospheric cloud tops to colder temperatures. For CTT ranging between –50 and –65 °C, the land results suggest a larger normalized frequency in the last years

(positive differences in Fig. 2f), while the oceanic results indicate a smaller one (negative differences in Fig. 2e).

The anomaly of normalized yearly area distributions for upper-tropospheric CTT (deviation from the 19-year mean; Fig. 2g–i) provides further details about the mentioned shift. Although the inter-annual variations are not negligible, we see a clear separation between the cyanish (representing the first years of data) and reddish (the last years) curves in the warmest and coldest CTT bins. This is especially prominent over land (Fig. 2i). The middle-top clouds with moderate CTT values show a mix of cyanish and reddish curves, indicating a considerable inter-annual variability most likely driven by short-term climate perturbations rather than long-term climate change. Overall, these results support a robust shift in upper-tropospheric clouds toward colder top temperatures throughout the study period.

For specifying the trend of climate warming, we analyze the evolution of the surface temperature, using atmospheric reanalysis data of Skin Temperature (ST, see Data in the Methods section for details). Figure 3a–c presents the time series of monthly ST anomalies (deviation from the 19-year mean of each month) averaged over the 3 domains (area-weighted; note the different ST scales). The most significant structural feature of these ST anomaly series, especially for the oceanic results (Fig. 3b), is the strong correlation with the Oceanic Niño Index (ONI, black lines, see ONI in the Methods section for details).

The ONI value is a common measure for the ENSO state[31]. Persistent large positive ONI-values indicate a warm phase of ENSO, i.e., El Niño, characterized by an unusual warming of the central and eastern tropical Pacific Ocean surface[32]. In contrast, persistent large negative ONI-values indicate the cold phase of ENSO, i.e., La Niña, the cooling counterpart of El Niño. As previously demonstrated, the ENSO is a dominant mode of climate variability on seasonal-to-interannual time scales, affecting the climate over a significant portion of the globe[33]. It propagates beyond the Pacific Ocean through atmospheric teleconnections[34] and influences temperatures and clouds globally[35–37]. The strong correlation between the ST anomaly series and the ONI series, as revealed in Fig. 3a–c is consistent with previous studies[35,36],
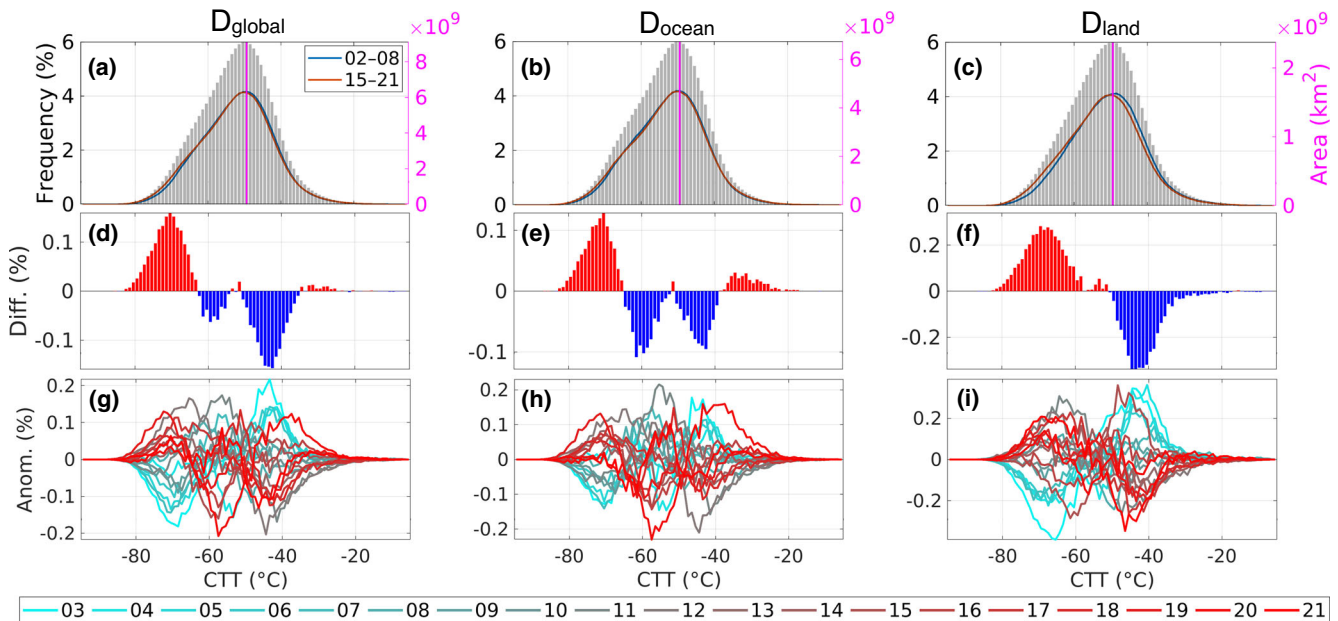
Fig. 2 Upper-tropospheric CTT distributions (in intervals of 1 °C) over D_{global} (left column), D_{ocean} (middle column), and D_{land} (right column), calculated using daily measurements. **a–c** The area distributions of CTT during 12.2002–11.2021 (gray bars, right magenta y-axis), and the normalized area distributions (the total area covered by upper-tropospheric clouds is divided to obtain the normalized frequency; left y-axis) during 12.2002–11.2008 (blue line) and 12.2015–11.2021 (red line); **d–f** the differences in the normalized area distributions between the last and first 6 years (12.2015–11.2021 minus 12.2002–11.2008); **g–i** anomalies of normalized area distributions (the corresponding 19-year mean of normalized frequency is subtracted to obtain the frequency anomalies) per year (from the December of the year before the legend year to the November of the legend year). The magenta line in panels **a–c** indicates the area distribution mode from 12.2002–11.2021. The red and blue bars in panels **d–f** mark positive and negative differences, respectively.

highlighting the major impact of El Niño and La Niña events on the global climate system[33,34].

Additionally, Fig. 3a–c shows that the ST anomaly series is a superposition of the ONI signal and a linear trend suggesting a signature of global warming[38]. It is worth noting that the ONI signal has no significant trend along the study period (0.0026 °C yr^{-1}, black dashed line in Fig. 3a). The linear trends are estimated by the ordinary least-squares (OLS) regression model (red lines in Fig. 3a–c, see OLS Regression in the Methods section). The results suggest warming rates of 0.02, 0.016, and 0.03 °C yr^{-1} over D_{global}, D_{ocean}, and D_{land}, respectively.

Similarly, but to a lesser extent, the ONI signal can be detected within the time series of monthly CTT anomalies (Fig. 3d–f), indicating the effect of ENSO on cloud properties[37,39]. More specifically, it demonstrates a warmer and colder CTT during El Niño and La Niña events. Thus we found a different ENSO signature on ST and CTT, which is associated with a different response of the two variables to the atmospheric and oceanic changes caused by the ENSO (Supplementary Fig. 1). As a consequence, examining CTT as a function of ST, on a near-global-scale, blurs the decreasing trend in CTT, as the ST is influenced more significantly by ENSO-related inter-annual variations than CTT (see Supplementary Figs. 1–2 and Supplementary Note 1 for details).

Nevertheless, the ENSO signature on the CTT anomaly series produces no significant bias on the clearly demonstrated decreasing trend. During the first two decades of the 21st century, the OLS regression model suggests a cooling rate of 0.052, 0.033, and 0.1 °C yr^{-1} in upper-tropospheric CTT over D_{global}, D_{ocean}, and D_{land}, respectively, constituting approximately 260%, 200%, and 330% of the magnitude of the corresponding warming rate in ST. We test the sensitivity of the trends shown here to the calculation method and the criterion used for determining the upper-tropospheric cloud subset and find them to be robust (see Cloud and Domain Classification in the Methods section, Supplementary

Fig. 3a–l, and Supplementary Note 2). We also observe a consistent decrease in high-level CTT measurements by the Atmospheric Infrared Sounder (AIRS) aboard the Aqua satellite (see Data in the Methods section, Supplementary Fig. 3m–o, and Supplementary Note 2 for details). Additionally, we find the decrease is associated with a non-isothermal lifting of cloud tops (i.e., the cloud tops are lifted in height more than the relevant isotherm in a warmer upper troposphere. See Supplementary Fig. 4 and Supplementary Note 3).

To better link our findings to the FAT hypothesis, which concerns mainly convective anvil temperature, we analyze the tropical (20° N–20° S; magenta dashed lines in Fig. 1b) anvil CTT estimations (Fig. 3g–i) based on MODIS observations (5 < ice COD < 30; see Data and Cloud and Domain Classification in the Methods section for details). The OLS regression model indicates a cooling rate of 0.045, 0.015, and 0.12 °C yr^{-1} in anvil CTT over D_{global}, D_{ocean}, and D_{land}, respectively. As previously observed for upper-tropospheric CTT, these results highlight clear disparities in CTT trends between land and ocean regions, with a much stronger decrease observed over land than over the ocean. However, even though the decreasing trend in anvil CTT over the ocean is relatively weak, it retains its statistical significance and constitutes approximately 94% of the magnitude of the corresponding warming rate in ST.

Moreover, by examination of the CTT trend as a function of cloud optical depth (COD; Fig. 3j–l), we are able to further distinguish between different upper-tropospheric clouds: thin anvils and cirrus (e.g., COD < 5), thick anvils (e.g., 5 < COD < 30), and deep convective cores (COD > 30)[11,15,40]. The consistent negative trends shown for all the COD bins suggest that the observed shift to colder CTT is a common feature of all the upper-tropospheric clouds. Specifically, deep convective cores exhibit an even stronger CTT decreasing trend, aligning with the recently reported increased frequency of extreme tropical deep convection under climate warming[41]. This higher frequency of extreme
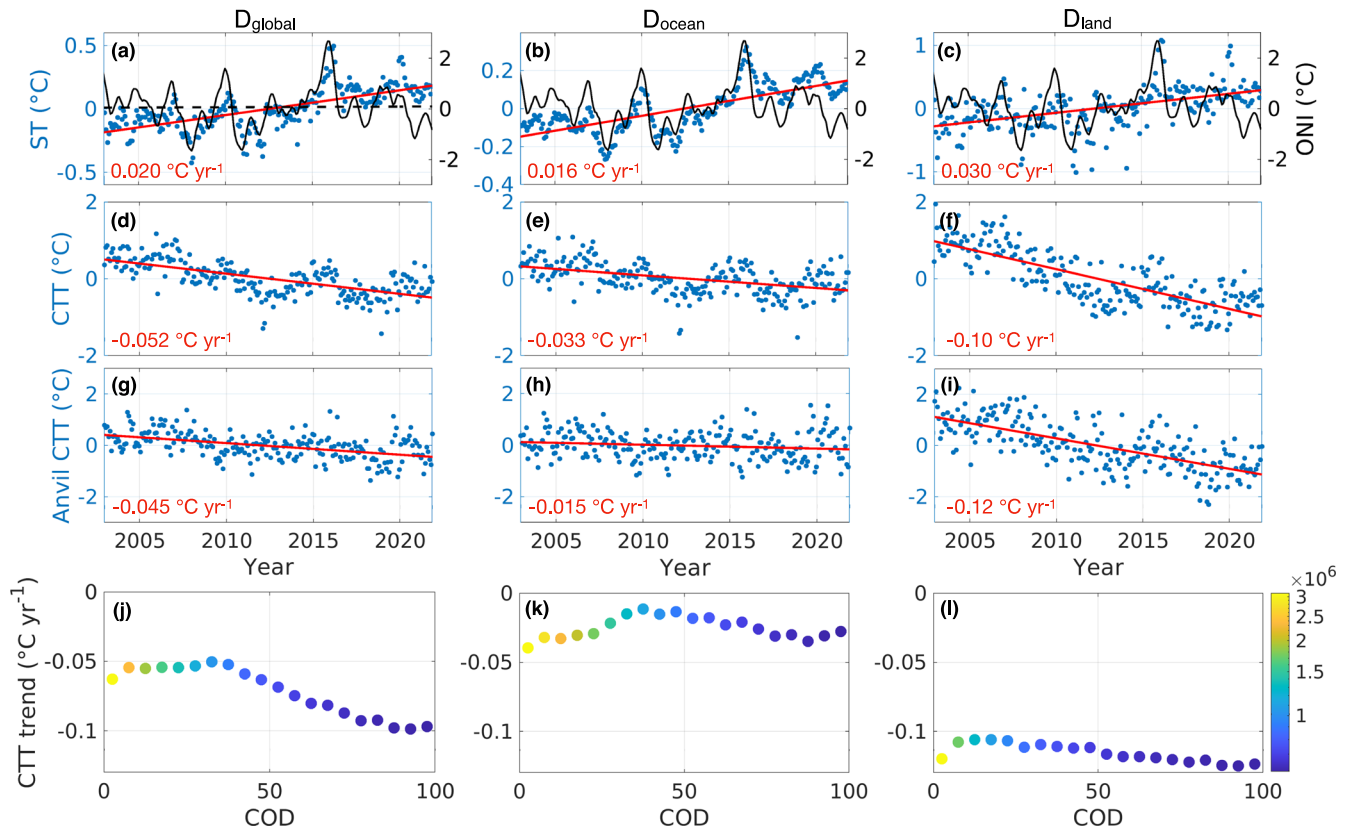
Fig. 3   Time series of spatially averaged monthly anomalies and CTT trends over D_{global} (left column), D_{ocean} (middle column), and D_{land} (right column). a–c ST anomalies (area-weighted, blue points) and ONI-values (black curve); **d–f** CTT anomalies (CF-area-weighted) for upper-tropospheric clouds; **g–i** CTT anomalies (CF-area-weighted) for anvil clouds over tropics (20° S–20° N; magenta dashed lines in Fig. 1b); and **j–l** linear trends in upper-tropospheric CTT anomalies as a function of COD (in intervals of 5) estimated by the OLS regression slope per COD bin. The black dashed line in panel **a** is the OLS regression line for ONI and is statistically insignificant at a 95% confidence level. In panels **a–i**, the red line is the OLS regression line for ST and CTT; the red number presents the corresponding linear trend estimated by the OLS regression slope. In panels **j–l**, the colors represent the total number of upper-tropospheric clouds per COD bin. All linear trends in ST and CTT are statistically significant at a 95 % confidence level.
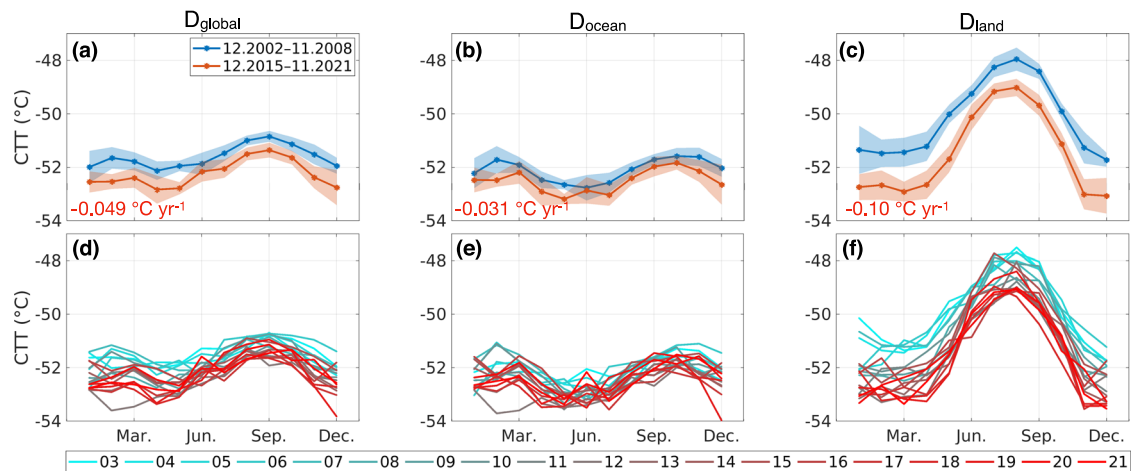

Fig. 4   Spatially averaged (CF-area-weighted) monthly upper-tropospheric CTT over D_{global} (left column), D_{ocean} (middle column), and D_{land} (right column). a–c Six-year means (dots) ± 1 s.d. (shades); and **d–f** monthly CTT of each year (from the December of the year before the legend year to the November of the legend year). The red number in **a–c** presents the linear trends estimated by the monthly differences' mean (red dots minus blue dots).

tropical deep convective clouds implies a larger contribution of the very cold CTT values to the upper-tropospheric CTT mean.

Next, we explore the upper-tropospheric CTT per month to examine the seasonality of the identified trends (Fig. 4). The means of the first and last 6 years of upper-tropospheric clouds

over land (Fig. 4c) show significantly colder CTT for the last years' dataset, suggesting that the revealed decreasing CTT trend is persistent throughout the year in all seasons. Similar to the linear trends estimated in Fig. 3d–f, the differences between the first and last years' CTTs suggest cooling rates of 0.049, 0.031, and 0.1 °C yr⁻¹
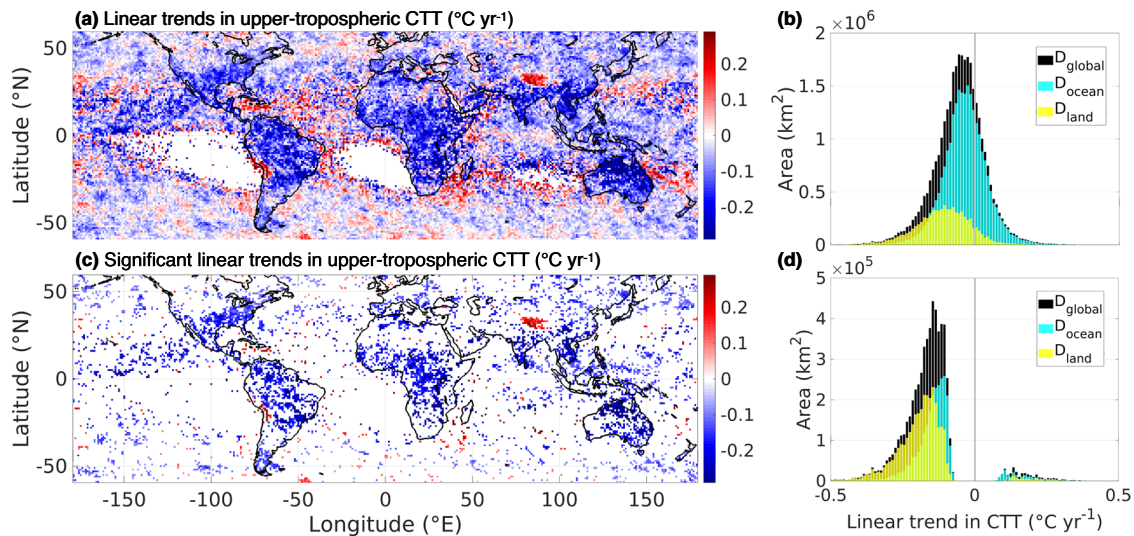
Fig. 5 Trend maps of upper-tropospheric CTT (unit: °C yr^{-1}) and the corresponding area distributions (CF-area-weighted summation, in intervals of 0.01 °C yr^{-1}), calculated using local monthly anomalies (CF-weighted) during 12.2002–11.2021. a A map of linear trends, estimated by the OLS regression slope per grid box (only areas with data over the entire 19 years are considered); **b** area distributions of the trends shown in **a**; **c** statistically significant trends at a 95 % confidence level; and **d** area distributions of trends shown in **c**. The black, cyan, and yellow bars in **b** and **d** are the results over D_{global}, D_{ocean}, and D_{land}, respectively.

in upper-tropospheric CTT over D_{global}, D_{ocean}, and D_{land}, respectively. Again, the decrease is less evident over the oceans (particularly in January, June, September, and October) than over land. The yearly results presented in Fig. 4d–f further demonstrate that the observed trend results from a gradual change during the study period rather than contributions from specific years. Another interesting finding is the seasonality of upper-tropospheric CTT and its opposite behavior over the ocean and land. Additional analysis suggests that these seasonality patterns are associated with the seasonal changes in atmospheric temperature and the asymmetric distribution of ocean and land between the two hemispheres (see Supplementary Fig. 5 and Supplementary Note 4 for details).

Finally, Fig. 5 presents a global map of the local linear trends in the CTT of upper-tropospheric clouds and the corresponding area distributions. These local trends (per grid box) are calculated as the slope of the OLS regression models predicting the time evolution of monthly CTT anomalies. A blue-dominated trend map (Fig. 5a) and the corresponding negative-dominated distributions (especially over land; Fig. 5b) suggest, once again, a dominant global feature of the observed decreasing trend in the upper-tropospheric CTT. This feature is very prominent when focusing on the statistically significant results (at a 95 % confidence level; Fig. 5c–d). One exception is the Tibetan Plateau, which exhibits an increasing CTT trend during the study period. A possible explanation is the extreme elevation of this region, which makes our cloud data definitions less valid. Nevertheless, the almost-universal decreasing CTT trend suggests robust and consistent cooling of the upper-tropospheric clouds' top. We suggest that climate warming and the resultant global changes are the most plausible explanations for the observed cooling patterns, as other known large-scale climate phenomena, such as the ENSO, the Pacific Decadal Oscillation, and the Atlantic Multi-decadal Oscillation, would most probably affect clouds by more complex and less homogeneous spatial modes[37].

Increase in upper-tropospheric water vapor concentration

The consistent decrease in upper-tropospheric (and specifically anvil) CTT shown here contradicts the prediction based on the FAT and PHAT hypotheses that suggested the upper-tropospheric CTT will remain almost fixed or increase slightly under climate

warming[5,6]. To explore the physical reasoning behind our results, we analyze the changes in water vapor mass mixing ratio (in g kg^{-1}) as a function of temperature level in the atmosphere.

The FAT theory assumes that the water vapor concentration depends mainly on temperature. Therefore, the anvil temperature, predominantly associated with the atmospheric level of the sharpest decrease in radiative cooling by clear-sky water vapor, should be nearly fixed at the temperature level at which the air is too cold to contain optically thick water vapor. However, the analysis of AIRS observations suggests a consistently increasing trend in clear-sky water vapor concentration (see Data and Cloud and Domain Classification in the Methods section for details) per temperature level in the upper troposphere during our study period (Fig. 6). In addition, a slightly stronger increasing trend is revealed over land (Fig. 6c) than over oceans (Fig. 6b). Although not fully explaining the observed decrease in upper-tropospheric CTT, it challenges the most fundamental assumption of the FAT hypothesis. If other links within the FAT hypothesis are true, such an elevated water vapor mixing ratio may shift the anvil layer to lower temperatures, consistent with the observed decrease in upper-tropospheric CTT and anvil CTT.

Potential radiative effect of upper-tropospheric clouds

To estimate the longwave radiative effect of the observed decrease in upper-tropospheric CTT, we explore the changes in the corresponding CF (see Supplementary Fig. 6 and Supplementary Note 5). A nearly constant mean CF (Supplementary Fig. 6b–d) suggests that the observed decrease in CTT is likely to drive more capture of thermal radiation; hence, an overall warming effect is expected. However, the local CF trends show spatial structures (Supplementary Fig. 6a). The weak decrease over the tropics and increase over higher latitudes suggest that more thermal radiation is trapped over mid-latitudes, and this effect may be compensated on some level by the CF reduction over the tropics, but we note the low significance of the CF analysis.

DISCUSSION

Adopting the FAT and PHAT hypotheses[5,6], almost all GCM simulations predict no changes or a very modest increase in upper-tropospheric CTT as the climate warms over the 21st
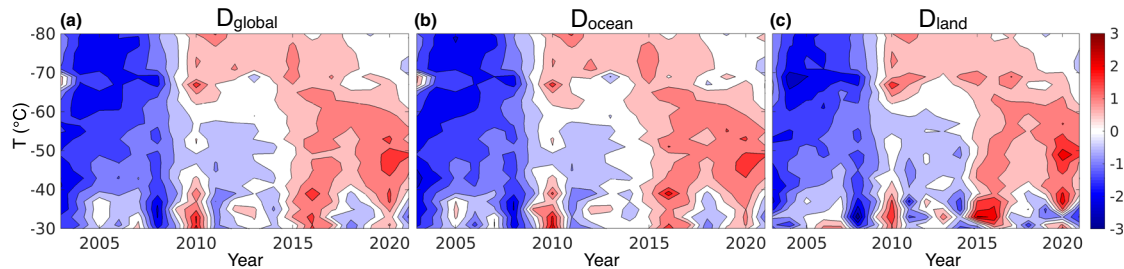
Fig. 6 Contour plots of the standard anomaly of clear-sky water vapor mass mixing ratio (unit: g kg^{-1}) over different domains, plotted against time (in 1 year intervals, from December to the following November) and clear-sky atmospheric T (in 2 °C intervals) using local annual data. a D_{global}; **b** D_{ocean}; **and c** D_{land}. The water vapor mixing ratios and atmospheric T at pressure levels of 400, 300, 250, 200, 150, and 100 hPa from AIRS are considered. To aid visualization, we first subtract the mean water vapor mixing ratio per T bin to obtain the anomalies and then divide by the standard deviation of results over D_{global} to obtain the standard values.

century[6]. Assuming no changes in other cloud properties, it suggests extra heating by the unchanging cloud emission together with a warmer surface[2,4,6,42].

However, our analysis, which uses satellite observations of cloud properties during the first two decades of the 21st century (12.2002–11.2021), reveals an opposite trend. The upper-tropospheric CTT is shifting consistently to colder values throughout the globe, particularly over land. This cooling rate is several times larger than the observed warming rate of the global surface. This decrease in upper-tropospheric CTT is associated with a non-isothermal lifting of cloud tops and is supported by an increase in the clear-sky water vapor mixing ratio of the upper troposphere. Although a full explanation of such observed decrease in upper-tropospheric CTT and the corresponding land-ocean differences requires further in-depth investigation (e.g., a process-level understanding of the link between the relevant clouds and the global warming-induced changes in thermodynamics), our findings challenge the validity of the FAT and PHAT hypotheses and suggest additional trapped thermal energy within the Earth-atmosphere system due to the overall decreased CTT and barely changed CF of upper-tropospheric clouds. Moreover, the observed decrease in CTT is not captured in current GCM simulations for a future warmer climate, indicating important missed processes regulating upper-tropospheric clouds and consequently a potentially underestimated warming rate for climate projections.

We are aware that uncertainties may stem from the limitations of our observational dataset, and the indirect identification of anvil temperature, and there is no perfect way to decouple cloud response to climate warming from the response to other natural variability factors. Nevertheless, the consistent decrease in high-level CTT using the AIRS measurements further supports our findings. In summary, the consistently shifted CTT distributions, the decadal robust global trends, the almost-universal geographical distribution of this trend, and the observed increase in water vapor mixing ratio for given temperatures suggest a physically based cooling response of upper-tropospheric CTT to climate warming and the resultant global changes, which requires more in-depth research of the underlying mechanisms.

METHODS

Data

Three datasets are used in this work, spanning December 2002 to November 2021 (12.2002–11.2021):

(1) The monthly products of the 5th generation of Atmospheric Reanalysis data from the European Centre for Medium-Range Weather Forecasts (ERA5)[43]. They offer uniformly sampled atmospheric data validated as the most reliable for climate trend assessments[44]. The variables of land-sea mask (LSM), ST (the theoretical surface temperature that satisfies the surface energy

balance), sea surface temperature at single levels[45], and atmospheric temperature (T) at 450, 400, 350, 300, 250, 225, 200, 175, 150, 125, and 100 hPa are used[46]. The original horizontal resolution of ERA5 is 0.25°, but we resample it to 1° to maintain the same resolution as the cloud products.

(2) The level 3 (L3) daily product of MODIS aboard Aqua satellite (MYD08-D3-C61)[25]. It has a horizontal resolution of 1° and is derived from the 5 km × 5 km L2 orbital-swath products. We use the data between 60° S and 60° N to avoid retrieval problems related to the bright areas near the poles. Daytime data (solar zenith angle ≤85°) is chosen to ensure the availability of COD measurements. Consequently, observation time can be pinned down to ~13:30 (local solar time) from approximately 23° S to 23° N, and can shift by up to 100 min for regions located poleward of 23°[25]. In addition, the Aqua satellite hasn't drifted[26], and MYD08-D3-C6.1 is well-calibrated by multiple independent observations. Issues like sensor aging and unphysical patterns are also carefully corrected in MYD08-D3-C6.1[47].

We use the CF (Cloud_Fraction_Day_Mean), CTT (Cloud_Top_Temperature_Day_Mean), COD (Cloud_Optical_Thickness_Combined_Mean), minimal CTP (CTP_Min, Cloud_Top_Pressure_Day_Minimum), CTP-Max (Cloud_Top_Pressure_Day_Maximum), and joint histograms of COD and CTT for ice clouds (Ice_COD_CTT_J-Histo, Cloud_Optical_Thickness_Ice_JHisto_vs_Temperature) in the main analysis. In the supporting material, the cloud top height (CTH, Cloud_Top_Height_Day_Mean), maximal CTH (CTH-Max, Cloud_Top_Height_Day_Maximum), and minimal CTT (CTT-Min, Cloud_Top_Temperature_Day_Minumum) are used. Parameters with the name suffix "Mean" are computed by taking an unweighted average of the L2 data in each L3 grid box; those with the name suffix "Maximum"/"Minimum" are defined as the maximum/minimum value of the L2 data in each L3 grid box. The Ice_COD_CTT_JHisto contains L2 pixel counts showing the distribution by comparing COD (12 bins bounded by 0, 0.5, 1, 2.5, 5, 7.5, 10, 15, 20, 30, 50, 100, 150) against CTT (13 bins bounded by 190, 200, 210, 220, 225, 230, 235, 240, 245, 250, 255, 260, 265, 270 K) for ice clouds. For mid to high-level clouds (e.g., we focus on upper-tropospheric clouds), Cloud top pressure (CTP) is determined using the CO_2 slicing approach, and the CTT/CTH is calculated based on the CTP using meteorological profiles[25]. The CO_2 slicing technique has been widely applied in cloud top properties retrievals, and is most sensitive to high clouds.

(3) The L2 daily and L3 monthly product from AIRS, aboard the Aqua satellite (L2_Daily_RetStd and L3_Monthly_RetStd, Version 7)[48,49], with a horizontal resolution of 1°. In the main analysis, the atmospheric T (Temperature_TqJ_A) and the water vapor mass mixing ratios (H2O_MMR_TqJ_A) at 400, 300, 250, 200, 150, and 100 hPa from L2_Daily_RetStd are used. The high-level CTT (CoarseCloudTemp_TqJ_A) from L3_Monthly_RetStd is used in the supporting material. The name suffix "TqJ_A" of the parameters indicates data collected during the ascending orbit (daytime,

except near the poles), with the collective quality control being used across all fields and levels.

Cloud and domain classification

To provide a latitude-following standard that captures a nearly normal CTT distribution, we define in the main analysis upper-tropospheric clouds as daily measurements with CF > 0 and CTP-Max ≤450 hPa. Measurements not identified as upper-tropospheric clouds are considered 0 for calculating upper-tropospheric CF but are ignored for calculating upper-tropospheric CTT and CTH (used in the supporting material). To evaluate the sensitivity of our findings to the definition of upper-tropospheric clouds, we conduct a complimentary analysis, presented in the supporting material, defining the upper-tropospheric clouds as daily measurements with CF > 0 and CTT-Max ≤ –20 °C, and with CF > 0 and CTH-Min ≥6 km. The local (per grid box) monthly cloud properties are then calculated as CF-weighted means of daily measurements. The CF weighting is performed to reduce the contribution of samples with smaller cloud coverage. The local monthly anomalies used for calculating domain averages and trend estimations are the deviation of local monthly data from the means of each given month over the whole study period.

To examine more closely the trend in convective anvil CTT, which is regarded in the FAT hypothesis, we employ a specific subset of anvil clouds, defined by using the Ice_COD_CTT_JHisto. Per the grid box, ice pixels with COD values ranging between 5 and 30 (corresponding to the 5th–9th COD bins) are classified as anvil clouds. The chosen COD thresholds are based on previous studies[11,15,40], and our results are not sensitive to these thresholds (checked, not shown). Then, we estimate the local anvil CTT as the Ice_COD_CTT_JHisto-weighted mean of the CTT bins (central values: 195, 205, 215, 222.5, 227.5, 232.5, 237.5, 242.5, 247.5, 252.5, 257.5, 262.5, and 267.5 K) that regard the anvils COD chosen bins. The local anvil CF is calculated as the product of the local CF and the fraction of anvils out of the clouds in the pixel. In addition, to assess the water vapor concentration (for validation of the FAT), we identified the clear-sky atmospheric T and water vapor mass mixing ratio, in daily measurements obtained for days with no clouds (CF = 0) and for cloudy days with no upper-tropospheric clouds (CF > 0 and CTP-Min > 450 hPa). The local monthly data is initially calculated based on these clear-sky daily measurements and then used to calculate the local annual data (Fig. 6).

To account for the clear distinction in climate trends between the land and oceans, we conduct separate analyses for D_{global}, D_{ocean}, and D_{land}. D_{global} is determined from 60° S to 60° N. D_{ocean} is defined as grid boxes with LSM-values ≤ 0.2 between 60° S and 60° N, while D_{land} is defined as grid boxes with LSM-values > 0.2 between 60° S and 60° N. Since the area of each 1° × 1° grid box depends on latitude, we performed an area weighting for the calculation of any spatial averages (area-weighted). The area of each grid box is estimated as the product of arc length at the corresponding latitude and longitude by regarding the Earth as an oblate spheroid with a radius of 6378.137 km at the equator and 6356.752 km at the poles. In addition, we incorporate CF weighting (CF-area-weighted) to account for the dependence on the cloud coverage when analyzing spatially averaged values of cloud top properties (and summed areas in Fig. 5b, d). For these spatial averages (and summations in Fig. 5b, d), the CF weights are computed as the CF climatology for a specific cloud subset, throughout the entire study period (e.g., the CF weights for upper-tropospheric clouds that were determined using a threshold on the CTP-Max, as presented in the main text, are given in Fig. 1a).

Oceanic Niño Index (ONI)

To identify and measure the state of ENSO, we calculated the ONI[31]. It is defined here as the 3-month running mean of the sea surface temperature anomaly over the Niño 3.4 region (5° N–5° S and 170° W–120° W, area-weighted). For each month, the corresponding average of 1950–2021 is subtracted from the monthly sea surface temperature data (deseasonalization) before calculating the ONI.

OLS regression

We perform the OLS regression to estimate the linear trend in the ST and CTT series[50]. The statistical significance of the corresponding trend (the OLS regression slope) is assessed by checking whether it is significantly different from zero at a confidence level of 0.95. Hence, a trend identified as significant in this work can be approximately considered as having a p-value < 0.05. The underlying regressions are performed with Matlab using the function 'fit' with the 'robust' option to exclude potential biases from outliers. The statistical significance of trends is estimated in Matlab by the function of 'confint'.

REFERENCES

1. Stephens, G. L. et al. An update on Earth's energy balance in light of the latest global observations. *Nat. Geosci.* **5**, 691–696 (2012).
2. Forster, P. et al. *The Earth's Energy Budget, Climate Feedbacks, and Climate Sensitivity, in Climate Change 2021: The Physical Science Basis. Contribution of Working Group I to the Sixth Assessment Report of the Intergovernmental Panel on Climate Change* (Cambridge University, 2021).
3. Gettelman, A. & Sherwood, S. C. Processes responsible for cloud feedback. *Curr. Clim. Change Rep.* **2**, 179–189 (2016).
4. Ceppi, P., Brient, F., Zelinka, M. D. & Hartmann, D. L. Cloud feedback mechanisms and their representation in global climate models. *WIREs Clim. Change* **8**, e465 (2017).
5. Hartmann, D. L. & Larson, K. An important constraint on tropical cloud-climate feedback. *Geophys. Res. Lett.* **29**, 12–1–12–4 (2002).
6. Zelinka, M. D. & Hartmann, D. L. Why is longwave cloud feedback positive? *J. Geophys. Res. Atmos.* **115**, D16117 (2010).
7. Seeley, J. T., Jeevanjee, N. & Romps, D. M. FAT or FiTT: are anvil clouds or the tropopause temperature invariant? *Geophys. Res. Lett.* **46**, 1842–1850 (2019).
8. Romps, D. M. An analytical model for tropical relative humidity. *J. Clim.* **27**, 7432–7449 (2014).
9. Thompson, D. W., Bony, S. & Li, Y. Thermodynamic constraint on the depth of the global tropospheric circulation. *Proc. Natl Acad. Sci. USA* **114**, 8181–8186 (2017).
10. Tompkins, A. M. & Craig, G. C. Sensitivity of tropical convection to sea surface temperature in the absence of large-scale flow. *J. Clim.* **12**, 462–476 (1999).
11. Li, Y., Yang, P., North, G. R. & Dessler, A. Test of the fixed anvil temperature hypothesis. *J. Atmos. Sci.* **69**, 2317–2328 (2012).
12. Saint-Lu, M., Bony, S. & Dufresne, J. L. Observational evidence for a stability iris effect in the tropics. *Geophys. Res. Lett.* **47**, e2020GL089059 (2020).

13. Xu, K.-M. et al. Statistical analyses of satellite cloud object data from CERES. Part II: tropical convective cloud objects during 1998 El Niño and evidence for supporting the fixed anvil temperature hypothesis. *J. Clim.* **20**, 819–842 (2007).

14. Zelinka, M. D. & Hartmann, D. L. The observed sensitivity of high clouds to mean surface temperature anomalies in the tropics. *J. Geophys. Res. Atmos.* **116**, D23103 (2011).

15. Kubar, T. L., Hartmann, D. L. & Wood, R. Radiative and convective driving of tropical high clouds. *J. Clim.* **20**, 5510–5526 (2007).

16. Eitzen, Z. A., Xu, K. M. & Wong, T. Cloud and radiative characteristics of tropical deep convective systems in extended cloud objects from CERES observations. *J. Clim.* **22**, 5983–6000 (2009).

17. Chae, J. H. & Sherwood, S. C. Insights into cloud-top height and dynamics from the seasonal cycle of cloud-top heights observed by MISR in the West Pacific Region. *J. Atmos. Sci.* **67**, 248–261 (2010).

18. Igel, M. R., Drager, A. J. & Van Den Heever, S. C. A CloudSat cloud object partitioning technique and assessment and integration of deep convective anvil sensitivities to sea surface temperature. *J. Geophys. Res. Atmos.* **119**, 10515–10535 (2014).

19. Byrne, M. P. & O'Gorman, P. A. Trends in continental temperature and humidity directly linked to ocean warming. *Proc. Natl Acad. Sci. USA* **115**, 4863–4868 (2018).

20. Chepfer, H., Noel, V., Winker, D. & Chiriaco, M. Where and when will we observe cloud changes due to climate warming? *Geophys. Res. Lett.* **41**, 8387–8395 (2014).

21. Aerenson, T., Marchand, R., Chepfer, H. & Medeiros, B. When will MISR detect rising high clouds? *J. Geophys. Res. Atmos.* **127**, e2021JD035865 (2022).

22. Pagano, T. S. & Durham, R. M. Moderate resolution imaging spectroradiometer (MODIS). *Proc. SPIE Sens. Syst. Early Earth Obs. Syst. Platf.* **1939**, 2–17 (1993).

23. Justice, C. O. et al. The Moderate Resolution Imaging Spectroradiometer (MODIS): land remote sensing for global change research. *IEEE Trans. Geosci. Remote Sens.* **36**, 1228–1249 (1998).

24. Parkinson, C. L. Aqua: an earth-observing satellite mission to examine water and other climate variables. *IEEE Trans. Geosci. Remote Sens.* **41**, 173–183 (2003).

25. Platnick, S. et al. MODIS Atmosphere L3 Daily Product. https://doi.org/10.5067/MODIS/MYD08_D3.061 (NASA MODIS Adaptive Processing System, Goddard Space Flight Center, USA, 2015).

26. Mears, C. A. & Wentz, F. J. Sensitivity of satellite-derived tropospheric temperature trends to the diurnal cycle adjustment. *J. Clim.* **29**, 3629–3646 (2016).

27. Norris, J. R. & Evan, A. T. Empirical removal of artifacts from the ISCCP and PATMOS-x satellite cloud records. *J. Atmos. Ocean. Technol.* **32**, 691–702 (2015).

28. Houze, R. A. Jr, Rasmussen, K. L., Zuluaga, M. D. & Brodzik, S. R. The variable nature of convection in the tropics and subtropics: a legacy of 16 years of the Tropical Rainfall Measuring Mission satellite. *Rev. Geophys.* **53**, 994–1021 (2015).

29. Pepler, A. & Dowdy, A. A three-dimensional perspective on extratropical cyclone impacts. *J. Clim.* **33**, 5635–5649 (2020).

30. Liu, H., Koren, I., Altaratz, O. & Chekroun, M. D. Opposing trends of cloud coverage over land and ocean under global warming. *Atmos. Chem. Phys.* **23**, 6559–6569 (2023).

31. Glantz, M. H. & Ramirez, I. J. Reviewing the Oceanic Niño Index (ONI) to enhance societal readiness for El Niño's Impacts. *Int. J. Disaster Risk Sci.* **11**, 394–403 (2020).

32. Trenberth, K. E. The definition of El Niño. *Bull. Am. Meteorol. Soc.* **78**, 2771–2778 (1997).

33. Neelin, J. D. et al. ENSO theory. *J. Geophys. Res. Oceans* **103**, 14261–14290 (1998).

34. Taschetto, A. S. et al. *Enso Atmospheric Teleconnections*, in *El Niño Southern Oscillation in a Changing Climate* (American Geophysical Union, 2020).

35. Davey, M. K., Brookshaw, A. & Ineson, S. The probability of the impact of ENSO on precipitation and near-surface temperature. *Clim. Risk Manag.* **1**, 5–24 (2014).

36. Deser, C., Alexander, M. A., Xie, S. P. & Phillips, A. S. Sea surface temperature variability: patterns and mechanisms. *Annu. Rev. Mar. Sci.* **2**, 115–143 (2010).

37. Li, Y. et al. Pairwise-rotated EOFs of global cloud cover and their linkages to sea surface temperature. *Int. J. Climatol.* **41**, 2342–2359 (2021).

38. Eyring, V. et al. *Human Influence on the Climate System, in Climate Change 2021: The Physical Science Basis. Contribution of Working Group I to the Sixth Assessment Report of the Intergovernmental Panel on Climate Change* (Cambridge University, 2021).

39. Yang, Y. et al. Impacts of ENSO events on cloud radiative effects in preindustrial conditions: changes in cloud fraction and their dependence on interactive aerosol emissions and concentrations. *J. Geophys. Res. Atmos.* **121**, 6321–6335 (2016).

40. Zelinka, M. D. & Hartmann, D. L. Response of humidity and clouds to tropical deep convection. *J. Clim.* **22**, 2389–2404 (2009).

41. Aumann, H. H., Behrangi, A. & Wang, Y. Increased frequency of extreme tropical deep convection: AIRS observations and climate model predictions. *Geophys. Res. Lett.* **45**, 13530–13537 (2018).

42. Yoshimori, M., Lambert, F. H., Webb, M. J. & Andrews, T. Fixed anvil temperature feedback: positive, zero, or negative? *J. Clim.* **33**, 2719–2739 (2020).

43. Hersbach, H. et al. The ERA5 global reanalysis. *Q. J. R. Meteorol. Soc.* **146**, 1999–2049 (2020).

44. Gulev, S. K. et al. *Changing State of the Climate System, in Climate Change 2021: The Physical Science Basis. Contribution of Working Group I to the Sixth Assessment Report of the Intergovernmental Panel on Climate Change* (Cambridge University, 2021).

45. Hersbach, H. et al. *ERA5 Monthly Averaged Data on Single Levels from 1940 to Present*. https://doi.org/10.24381/cds.f17050d7 (Copernicus Climate Change Service (C3S) Climate Data Store (CDS), 2023).

46. Hersbach, H. et al. *ERA5 Monthly Averaged Data on Pressure Levels from 1940 to Present*. https://doi.org/10.24381/cds.6860a573 (Copernicus Climate Change Service (C3S) Climate Data Store (CDS), 2023).

47. Lyapustin, A. et al. Scientific impact of MODIS C5 calibration degradation and C6+ improvements. *Atmos. Meas. Tech.* **7**, 4353–4365 (2014).

48. AIRS project. *Aqua/AIRS L3 Daily Standard Physical Retrieval (AIRS-only) 1 degree × 1 degree V7.0*. https://doi.org/10.5067/UO3Q64CTTS1U (Goddard Earth Sciences Data and Information Services Center, 2019).

49. AIRS project. *Aqua/AIRS L3 Monthly Standard Physical Retrieval (AIRS-only) 1 degree × 1 degree V7.0*. https://doi.org/10.5067/UBENJB9D3T2H (Goddard Earth Sciences Data and Information Services Center, 2019).

50. Wells, D. E. & Krakiwsky, E. J. *The Method of Least Squares* (University of New Brunswick, 1971).

AUTHOR CONTRIBUTIONS

H.L. conducted the analysis. All authors wrote the manuscript and approved its final form.

COMPETING INTERESTS

The authors declare no competing interests.

ADDITIONAL INFORMATION

Supplementary information The online version contains supplementary material available at https://doi.org/10.1038/s41612-023-00465-5.

Correspondence and requests for materials should be addressed to Ilan Koren.

Reprints and permission information is available at http://www.nature.com/reprints

Publisher's note Springer Nature remains neutral with regard to jurisdictional claims in published maps and institutional affiliations.